Calibration data for this five-hole probe was obtained by Drost (37). Figure 3.11 presents the calibration data for the five-hole probe. The calibration range was ±40° in both the yaw and pitch planes, although for clarity Figure 3.11 only depicts yaw angles out to ± 34°. The data was represented by cubic spline curves passed through the individual data points, a technique described in Appendix D. Wall proximity effects were neglected for the five-hole probe due to the lack of necessary measurements in this region as well as the relatively flat response of the pressure coefficients to wall proximities greater than 0.276 inches (0.007 m). Reynolds number effects were also neglected due to the pressure coefficients being weakly dependent on velocity or Reynolds number (36).

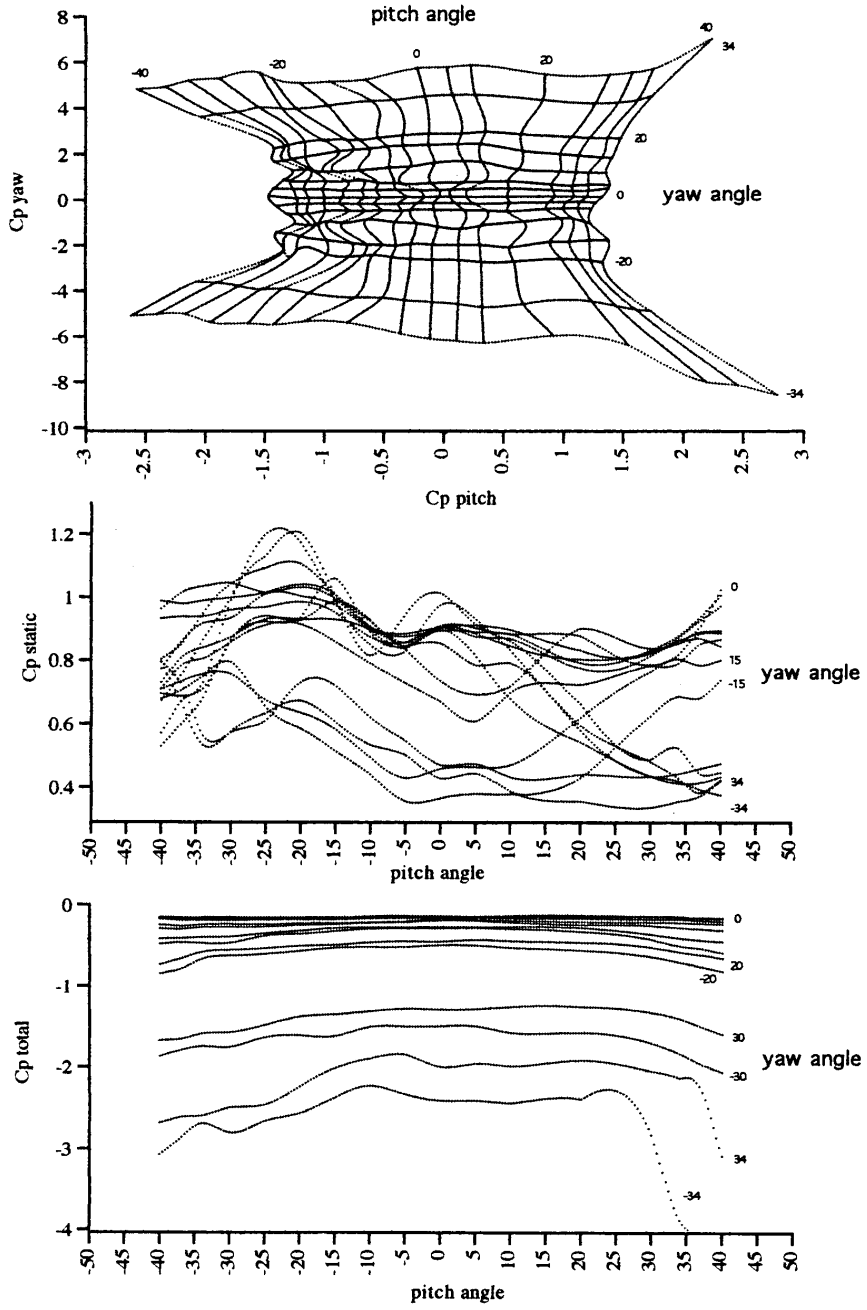

Figure 3.11: Calibration Curves for Five-Hole Pressure Probe (37).

The five-hole probe was aligned with the compressor axis by preliminary testing in a low-speed wind tunnel with an attached protractor to determine the necessary probe

rotation offsets in the pitch and yaw planes to null it in a known axial flow (eg., $p_2 = p_3$, $p_4 = p_5$). The probe was then inserted in the compressor using the same offsets as determined in the wind tunnel. A schematic of the inlet and total pressure ratio measurement pneumatic probes and their installation with respect to the rotor is shown in Figure 3.12. A Pitot-static probe mounted at mid-span 6.8 chords or 11.5 inches (0.292 m) aft of the rotor was used to measure downstream total pressure, and therefore total pressure rise across the fan relative to atmospheric. Flexible Tygon tubing connected the pressure probes to a Scanivalve model W1260/12P-12T fluid switch wafer and WS5 12 solenoid drive stepped by a Scanivalve model CTLR10P/S2-S6 solenoid controller. Pressures were then measured by a Datametrics Barocel Type 590D-10W-2P1-V1X-4D Transducer and Type 1400 Electronic Manometer. This arrangement allowed pressure measurements accurate to 0.001 inches (2.54×10^{-3} cm) of H_20 with a differential range of 10.0 inches (25.4 cm) of H_2O. Data was read into and averaged by a LabView virtual instrument **mean.vi**.

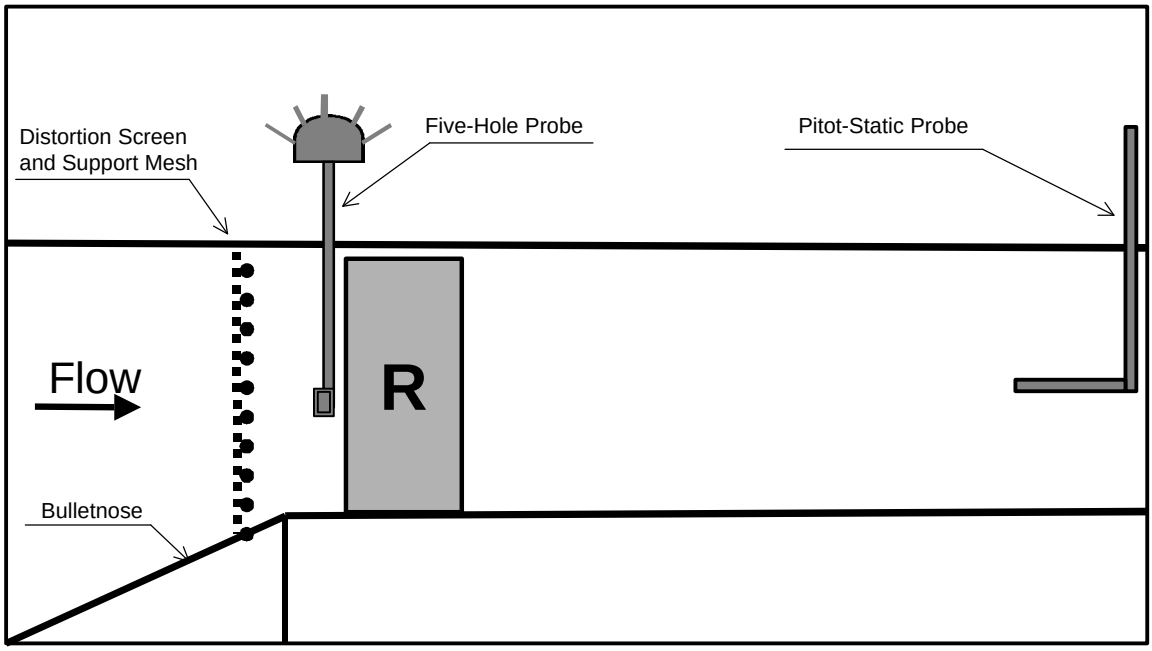

Figure 3.12: Pneumatic Probes Relative to Rotor in Meridional Plane.

One-dimensional wake data was obtained using a piggyback steady/unsteady total pressure probe located 0.2 C or 0.334 inches (0.848 cm) downstream of the rotor. A schematic of this probe is presented in Figure 3.13. The manufacturer's specification diagram for the Entran transducer contained in the probe is shown in Figure 3.14.

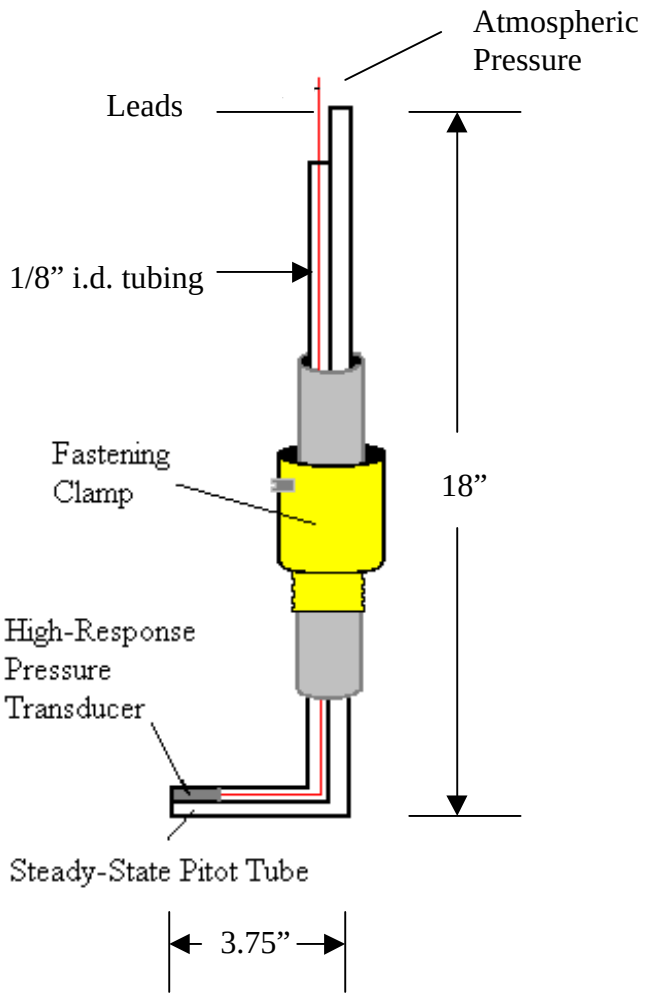

Figure 3.13: Diagram of Piggyback Steady/Unsteady Total Pressure Probe.

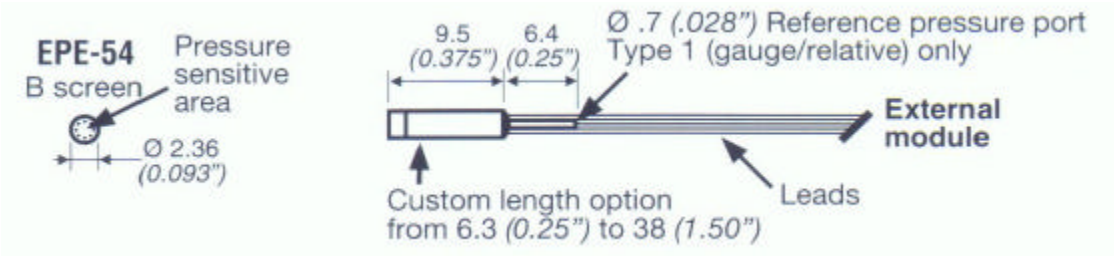

Figure 3.14: Diagram of High-Response Entran Pressure Transducer.

The position of the combination probe located 0.2 chords downstream of the rotor is shown in Figure 3.15.

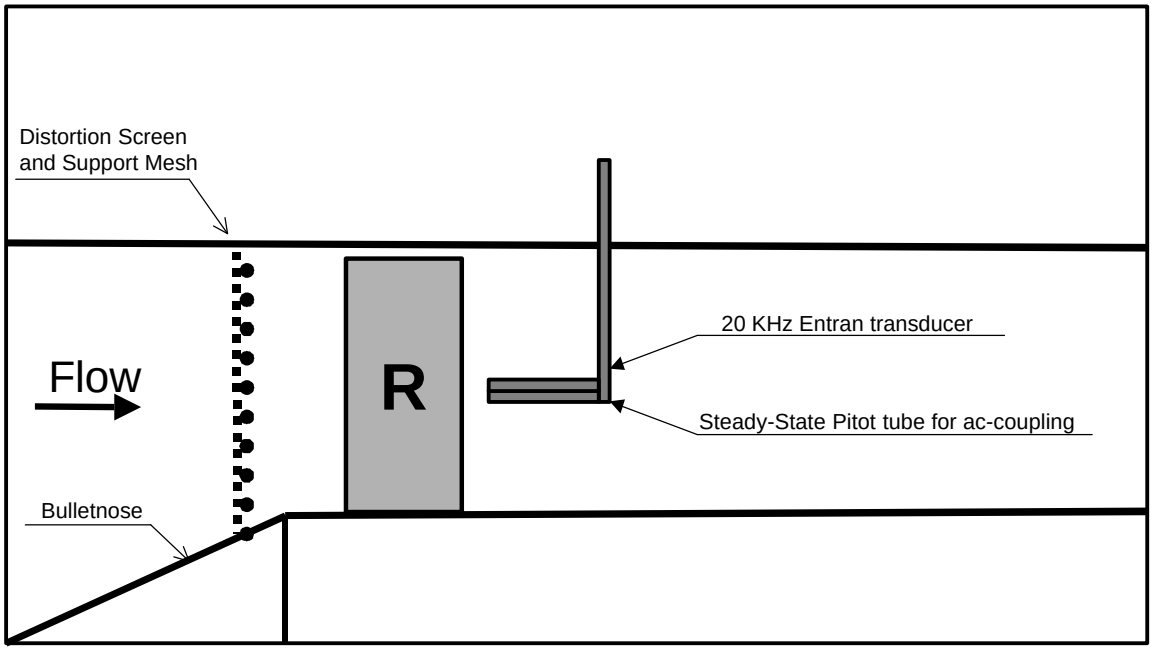

Figure 3.15: Diagram of Steady/Unsteady Probe Relative to Rotor.

A high-pass RC analog filter with –3 dB cutoff at 1.6 Hz was applied to the transducer output. Dynamic total pressure data was not low-pass filtered to eliminate aliasing about the Nyquist frequency of 10 kHz due to the rapidly decreasing energies approaching 10 kHz, as shown in Figure 3.16. The power spectrum shown in Figure 3.16 was obtained using a MATLAB zero-padding FFT sequence length of order $2^{12} = 4096$. During the actual testing, a spectrum analyzer confirmed an extremely low noise floor attenuated 40 dB above 10 kHz.

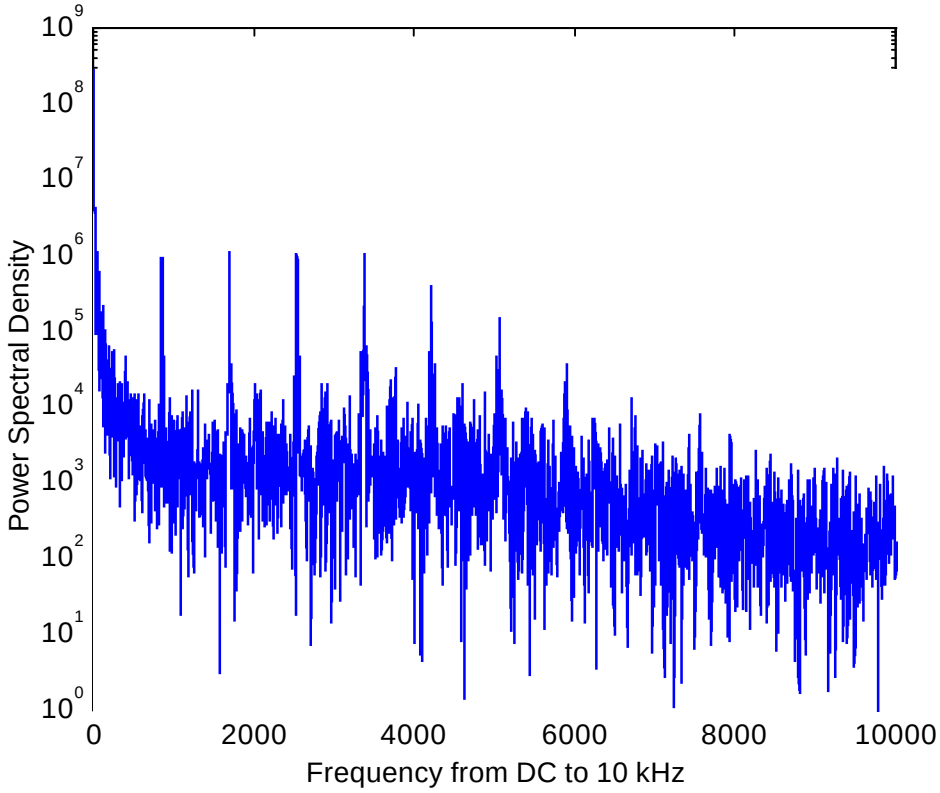

Figure 3:16: Power Spectral Density of Sample Unsteady Total Pressure.

One-per-rev, downstream steady-state, and transducer unsteady total pressures were sampled by the computer at 20 kHz for 0.12 seconds using a LabView virtual instrument **mod4.vi**. The data acquisition system consisted of a Gateway P166 laptop with a National Instruments DAQCard-AI-16E-4 I/O card as described in Appendix C. The rotor rotational speed was measured using a Hewlett Packard 5315A 100 MHz Universal Counter attached to a one-per-rev signal from the rotor.

3.2 Summary of Experiments

The first experiment involved obtaining the rotor characteristics as shown in Figure 3.17. These were obtained by running the machine at a constant speed of 2100 rpm with the low-solidity support mesh installed by itself without a distortion screen, and then with each of the Level 1, Level 2, and Level 3 distortion screens. In addition, the characteristic for the undistorted rotor was measured with the low-solidity support mesh in place to be used as a reference characteristic.

The rotor characteristics were obtained by plotting the non-dimensional pressure rise Ψ vs. the velocity coefficient C_x/U_{tip} as shown in Figure 3.17, where the non-dimensional pressure rise Ψ is defined by

$$\Psi = \frac{P_{ann} - P_{atm}}{\frac{\rho \cdot U_{tip}^{2}}{2}} \qquad \textbf{(3.5)}$$

where P_{ann}, P_{atm}, ρ, U_{tip}, and C_x are annulus total pressure, atmospheric pressure, air density, blade tip velocity, and axial velocity, respectively. The annulus total pressure P_{ann} was found to be identical to the plenum static pressure obtained using a wall tap, which should be true for a low-speed machine.

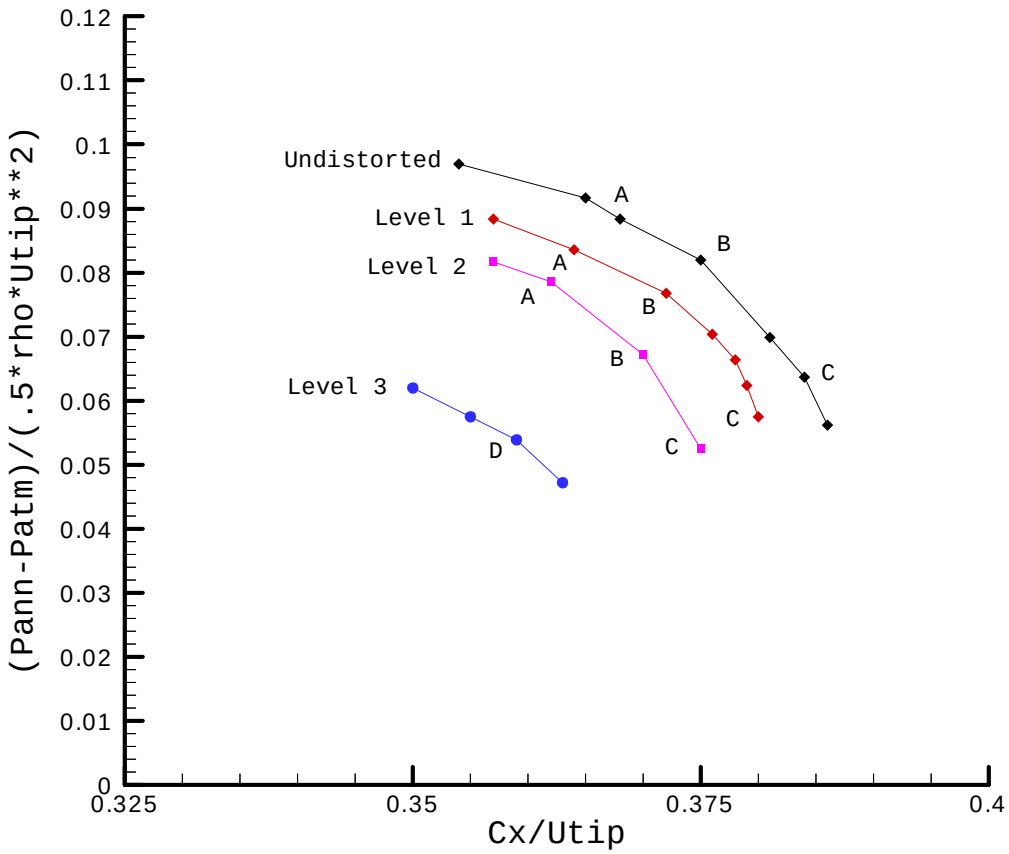

Figure 3.17: Distorted and Undistorted Low-Speed Axial-Flow Fan Performance Characteristics.

The flow coefficient was varied by use of the controlled throttle plate at the exit of the plenum chamber. The mass rate of flow was measured using the inlet Pitot-static and probe rakes. The rotor inlet total pressure was assumed to be ambient by neglecting losses through the inlet duct. For the case of an undistorted rotor with only the support mesh installed, rotating stall inception occurred at a steady-state stalling angle of attack of 12.6º as measured by the five-hole probe at 50 % span. Note how the rotor characteristics indicate decreased rotor performance and flow rates for an increase in distortion intensity, with more intense distortions shifting the performance to progressively lower corrected rotor speeds.

The second set of experiments involved obtaining blade inlet flow angle and total and static pressure profiles using the five-hole pressure probe. Rotor flow data was obtained for a 270° circumferential profile, which exceeded the fraction of the inlet which would experience the direct influence of the various 110° distortion screens. The rotor inlet flow survey was performed with 30° resolution about the 270° circumference of the annulus which the stationary five-hole probe experienced relative to the rotatable distortion.

Blade inlet data was taken at 33%, 50%, and 67% spans at operating points A, B, C, and D for the screen levels noted in Figure 3.17. Due to its limited characteristic, only data for operating point D were attainable for the Level 3 screen. Blade loading increases as one moves up the speed line, with the pre-stall conditions at point A.

The third set of experiments involved the blade wake survey corresponding to the inlet flow measurements at 33%, 50%, and 67% spans for operating points A, B, C, and D for the screen levels noted in Figure 3.17. Again, only operating point D was surveyed for the Level 3 screen. The five-hole pressure probe was removed from the rotor inlet prior to obtaining downstream wake data to avoid flow interaction between probes. The rotor exit flow survey was performed with 10° resolution about the 270° circumference of the annulus which the steady/unsteady piggyback probe experienced relative to the rotatable distortion. Data resulting from the third set of experiments are shown in Chapter 4 and Appendix A.

3.3 Instrumentation Setup and Calibration

The Barocel micromanometers were calibrated against an inclined manometer containing red gauge oil. A linear regression was used to obtain the line fitting of calibration data, as shown in Figure 3.18.

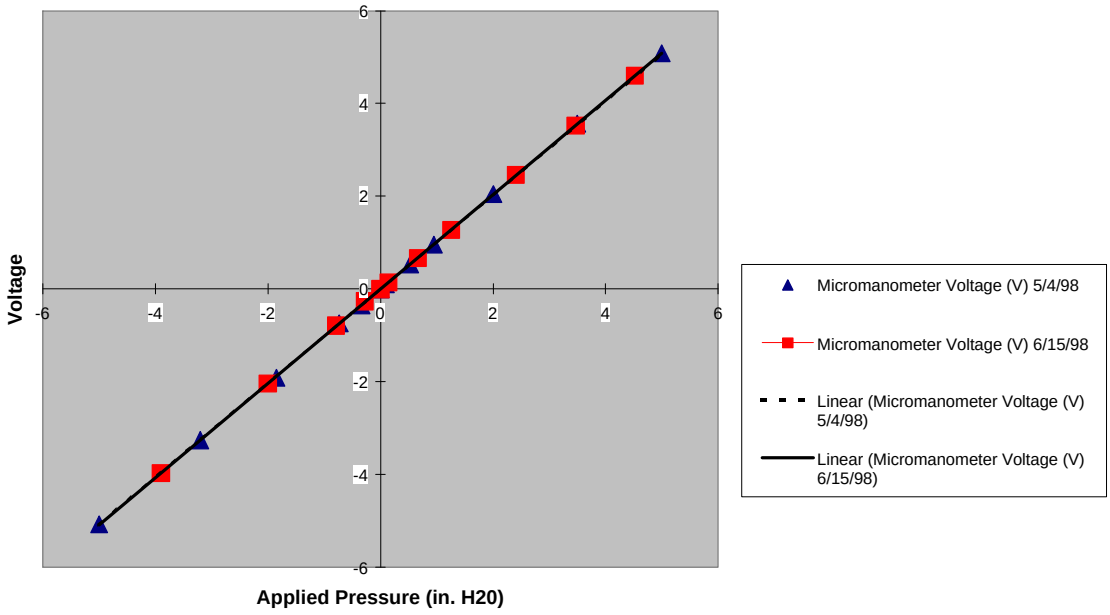

Figure 3.18: Plot of Micromanometer Response for Two Independent Calibrations.

The pressure transducer output was assumed to follow the manufacturer's calibration of 77.0 mV/psig. Amplifier gain was checked by unhooking the lead from the transducer and applying a known voltage before and after the amp, then reading the corresponding output voltages on an oscilloscope.

3.4 Data Acquisition and Processing

Measurements from the five-hole pneumatic probe for steady inlet data were recorded at a sampling rate of 2 Hz for 30 seconds. Unsteady flow effects at the inlet were assumed negligible as compared to the rapid blade passing frequency behind the five-hole probe. This amount of data was deemed adequate, as additional sampling time did not modify the time mean by more than 2 %. The five-hole probe data allowed calculation of the three-dimensional inlet flow angles and magnitudes, as well as the total and static pressures at the inlet. Inlet flow angles are presented in Ch. 4 without modification. The inlet total and static pressures in Ch. 4 relative to the ambient were non-dimensionalized by blade tip wheel speed as shown in Equations **(3.6)** and **(3.7)**.

$$P_{static}\ \text{Rel} = (P_{static} - P_{amb}) / (\frac{1}{2}\rho \cdot U_{tip}^{2}) \qquad \textbf{(3.6)}$$

$$P_{total}\ \text{Rel} = (P_{total} - P_{amb}) / (\frac{1}{2}\rho \cdot U_{tip}^{2}) \qquad \textbf{(3.7)}$$

Unsteady wake data was obtained using the combination probe as described in Section 3.1.6. Data were sampled at 20 kHz for 0.12 seconds. Figure 3.19 depicts typical separate steady-state mean DC and unsteady AC total pressure components from the combination probe.

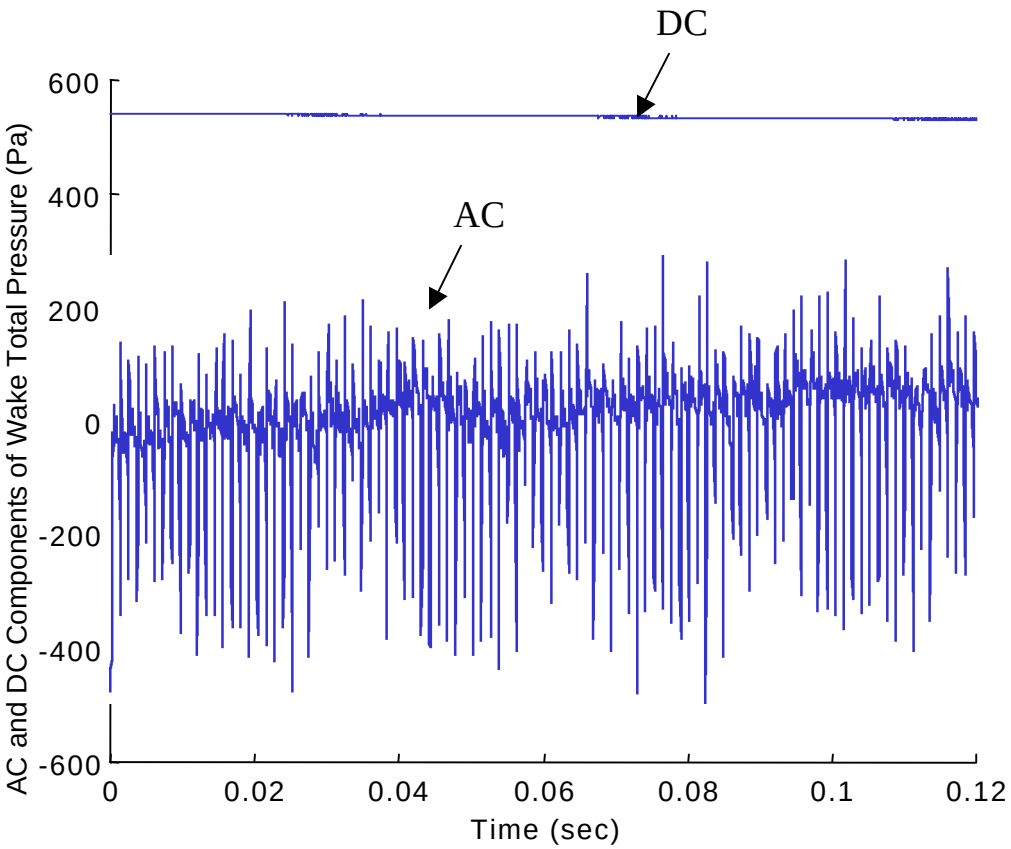

Figure 3.19: AC and DC Components of Total Pressure.

The unsteady AC and mean DC components were superimposed as shown in Figure 3.20 to obtain the complete unsteady total pressure profile downstream of the rotor. This allowed higher resolution of the voltage measurements by minimizing the channel voltage input range in the data acquisition routine **mod4.vi** for the transducer output signal to ± 1.0 V. Channel voltage ranges for the steady total pressure signal and the one-per-rev signal measurements were ± 5.0 V.

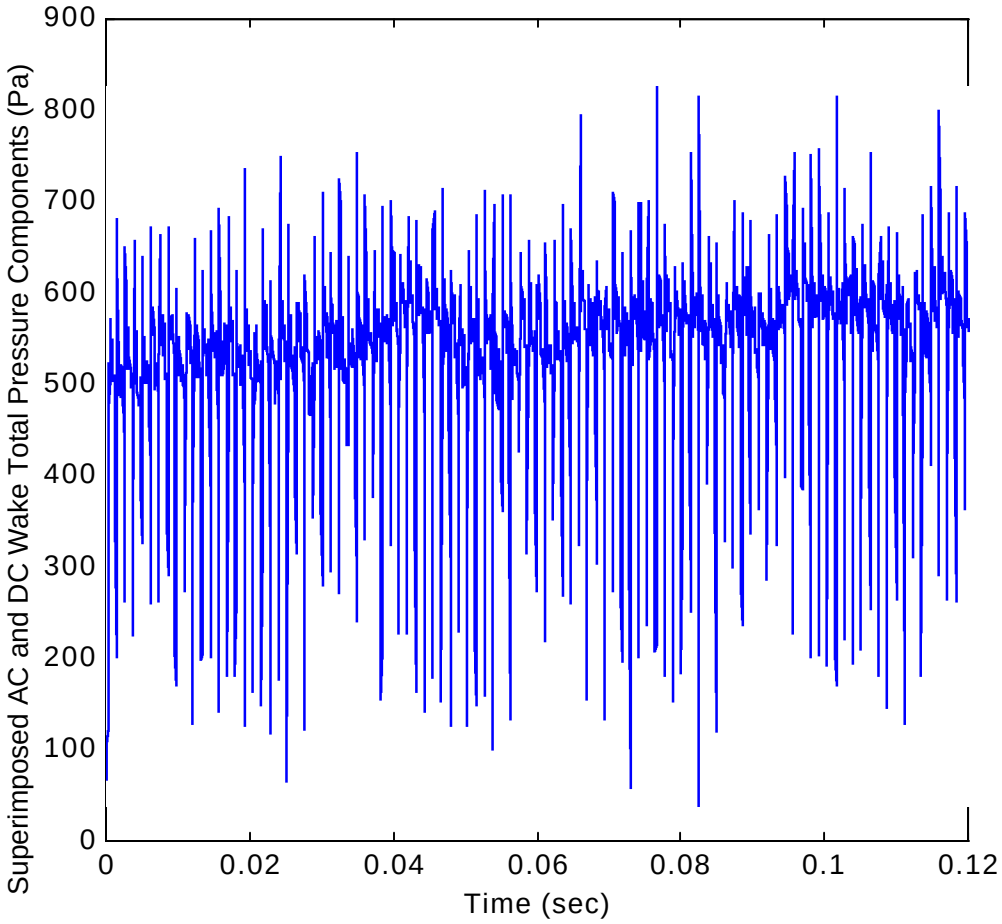

Figure 3.20: Superimposed AC and DC Components of Total Pressure.

Given the blade passage time of roughly 1.2 msec and the sampling time of 0.12 seconds, these data sets corresponded to approximately 100 blade passings. Unsteady total pressure data was then phase-locked with a one-per-rev signal from the rotor as described below.

Figure 3.21 displays a time series of one-per-rev voltage outputs used for phase-lock averaging. The secondary peaks are due to the presence of a balancing washer on the shaft.

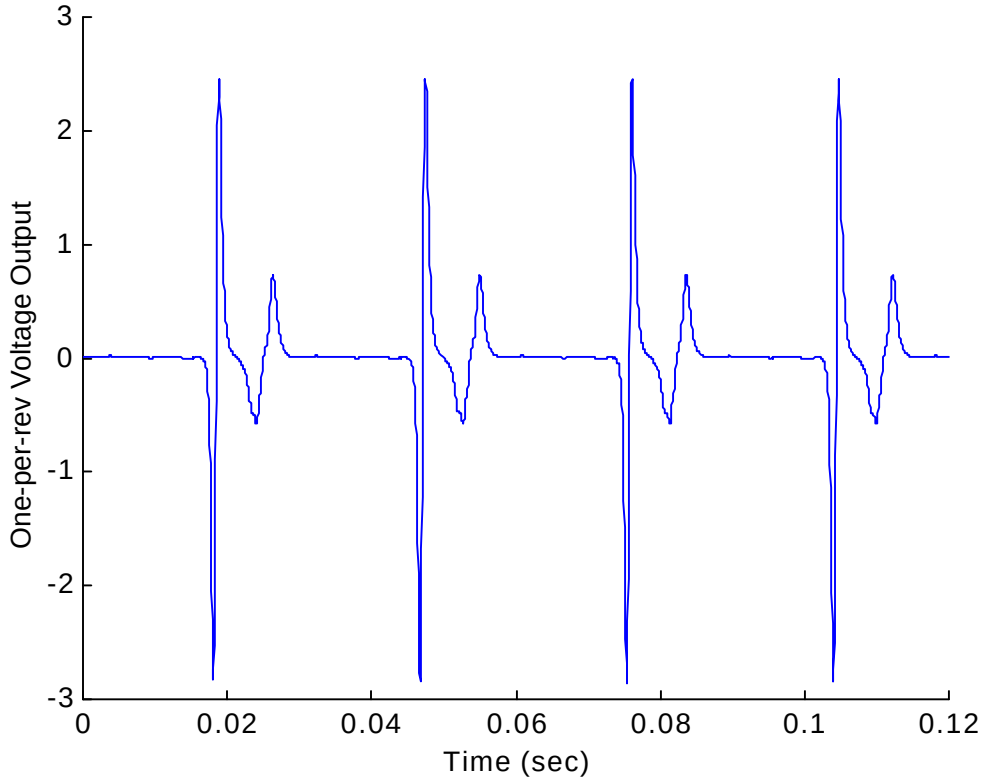

Figure 3.21: Time Series of One-per-rev Voltage Output Used for Phase-lock Averaging.

Using each of the positive voltage peaks to obtain the phase, the superimposed unsteady total pressure signal was divided into data blocks corresponding to the data taken between each of the four one-per-rev peaks, the beginning of which is shown in Figure 3.22. Four one-per-rev peaks allowed the capture of data for three full rotor rotations (or periods) and therefore a total of 72 blade passages. This number of blade passages was assumed satisfactory in order to provide an ensemble-average which was highly representative of the true one-dimensional blade exit flow. In order to ensemble-average the unsteady rotor exit data, it was assumed that the data were stationary.

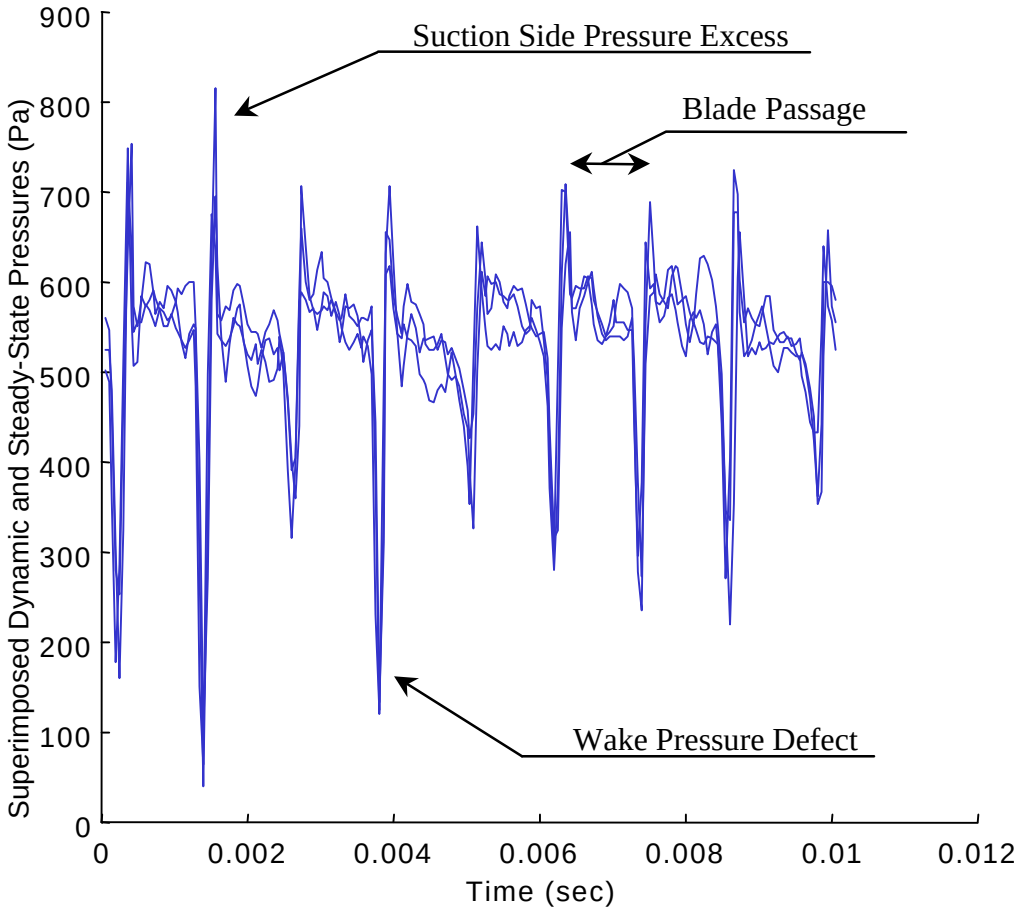

Figure 3.22: Sample of Ensemble Averaging of Three Wakes for Repeatability.

The three data blocks in Figure 3.22 were subsequently averaged to obtain a series of 24 unsteady rotor exit blade passes. This series of three passages of the same blades demonstrates excellent repeatability. It is interesting to note the considerable randomness of the suction side total pressure jets and freestream total pressures as seen in Figure 3.22. Wake characteristics such as thickness and maximum depth remain relatively constant for each individual blade passage.

Using the analysis of previous wake researchers as a foundation, a set of non-dimensional rotor exit flow parameters were calculated in order to describe the average total pressure width and depth for both the suction surface jet and the wake. As there was no longer any absolute phase information in the one-dimensional rotor exit flow total

pressure profiles, the non-dimensional parameters were computed for each of the 24 blade passes and then averaged once again. Figure 3.23 is a graphic of the analysis used for a sample blade passage.

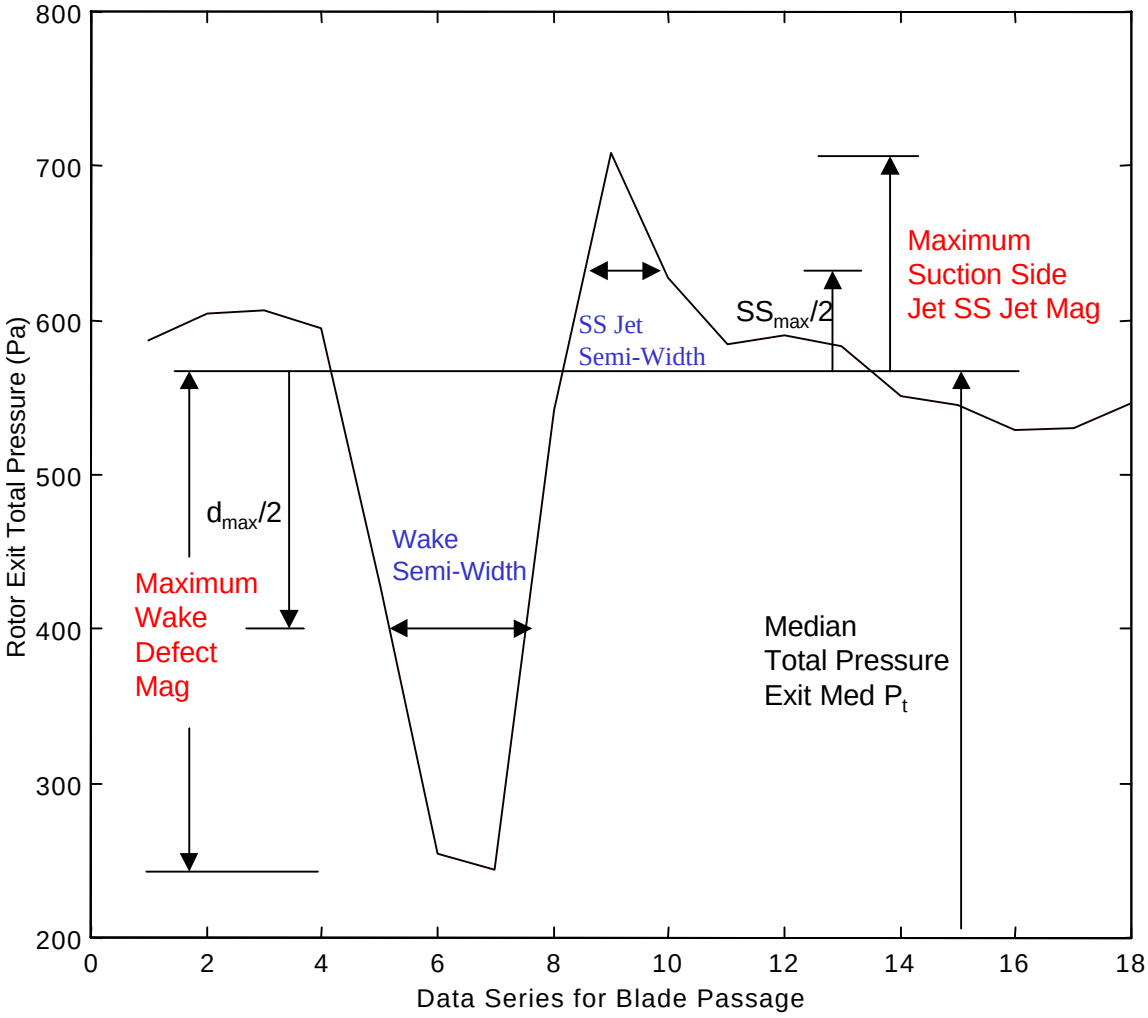

Figure 3.23: Exit Flow Parameters of Sample Blade Passage.

The total pressure suction side jet and wake defect were computed relative to the median of the superimposed total pressure signals Pt_{med}, which was judged to be a better approximation of the freestream velocity than the mean. These relative pressures for the

suction side jet and wake defect were then non-dimensionalized by blade tip wheel speed as presented in Equations **(3.8)** and **(3.9)**.

$$\text{SS Jet Mag} = (\text{SS Jet Max} - \text{Pt}_{\text{median}}) / \left(\frac{1}{2}\rho \cdot U_{tip}^{2}\right) \quad \textbf{(3.8)}$$

$$\text{Wake Defect Mag} = -1 * (\text{Pt}_{\text{median}} - \text{Wake Defect}_{\text{max}}) / \left(\frac{1}{2}\rho \cdot U_{tip}^{2}\right) \quad \textbf{(3.9)}$$

Suction side jet and wake semi-widths were converted from lengths to units of time and non-dimensionalized by the time Δt = 1.2 msec for a blade passage at 2100 rpm.

$$\text{SS Jet Semi-Width} = (\text{SS jet passage time} / \Delta t) \quad \textbf{(3.10)}$$

$$\text{Wake Semi-Width} = (\text{Wake width passage time} / \Delta t) \quad \textbf{(3.11)}$$

Linear interpolation was used to obtain the semi-widths for the suction side jet and the wake total pressure defect. The steady-state median exit total pressure was also non-dimensionalized by blade tip wheel speed as shown in Equation **(3.12)**.

$$\text{Exit Med Pt} = (\text{Pt}_{\text{steady-state}} - \text{P}_{\text{atm}}) / \left(\frac{1}{2}\rho \cdot U_{tip}^{2}\right) \quad \textbf{(3.12)}$$

Data in Chapter 4 are presented using cubic spline curve fitting techniques as described in Appendix D.